

## Tutorial

# Characterization study of deep-level defect spatial distribution, emission mechanisms, and structural identification

Zilan Wang<sup>\*</sup> , Jiapeng Yang and Haoyang Li

School of Optoelectronic Engineering and Instrumentation Science, Dalian University of Technology,  
Dalian 116024, People's Republic of China

E-mail: [wangzilan@dlut.edu.cn](mailto:wangzilan@dlut.edu.cn)

Received 4 March 2024, revised 14 June 2024

Accepted for publication 20 September 2024

Published 21 October 2024



## Abstract

The characterization of defects in semiconductor materials and devices is crucial for enhancing the performance and reliability of semiconductor products. This tutorial review focuses on deep level transient spectroscopy (DLTS) as the primary analytical tool, thoroughly discussing its distinct advantages in deep-level defect characterization. However, it is unable to reveal the concentration-depth distribution of deep-level defects, neglects the dependency of carrier emission rates on the electric field, and fails to accurately identify defect structures. To overcome these limitations, three enhanced DLTS techniques have been developed to extend the capabilities of DLTS. These enhancements include the utilization of graded filling pulse technology to accurately map defect distributions at various depths within devices, facilitating individual defect characterization across different layers of multilayered structures; the application of varying electric field strengths to samples to delve into the intricate physical mechanisms of defects during carrier emission processes; and the adjustment of the duration of electric pulse injection to monitor signal growth trends, deducing the microstructure of defects. The paper integrates research findings from a wide array of field experts, meticulously outlines a description of how to obtain the depth distribution of defect concentration in devices, furnishes quantitative criteria for both the Poole–Frenkel effect and phonon-assisted tunneling mechanisms of carrier emission, and provides specific examples for distinguishing between interface states/bulk defects and point defects/extended defects. This enhances both the theoretical and practical knowledge in this field. The advanced DLTS techniques outlined provide crucial guidance for defect characterization and performance optimization in semiconductor devices with new structures and materials.

**Keywords:** DLTS, defect characterization, concentration-depth distribution, carrier emission mechanisms, defect structure identification

---

<sup>\*</sup> Author to whom any correspondence should be addressed.

## 1. Introduction

One of the reasons semiconductors are extensively utilized in the production of electronic and optical devices is that their electronic properties can be altered by the introduction of a small amount of impurities or other defects. For instance, doping silicon crystals to fabricate *n*-type and *p*-type semiconductors can significantly modify their conductivity [1]. Similarly, selecting specific impurities can alter the material's band gap, enabling LEDs to emit light of various colors [2], among other applications.

In the fabrication of semiconductor materials, alongside the intentional introduction of beneficial defects, the formation of undesirable defects is also inevitable. These include impurities, native defects, and extended defects, among others, which significantly impact the performance and reliability of semiconductor devices. For example, dislocations or impurities in semiconductor crystals can capture electrons and holes, reducing the devices' current conductivity, which can result in current leakage and increased resistance [3]. In the realm of high-speed electronics and high-frequency communications, device performance is significantly impacted by these defects. For instance, lattice constant mismatches in high electron mobility transistors cause discontinuities in the conduction band and deep-level traps, diminishing device performance [4, 5]. These deep-level traps, by capturing charge carriers, increase signal noise and can cause interference effects, affecting the normal output of the device. This can lead to signal disturbances that may last up to milliseconds [6].

In the field of optoelectronic devices, such as LEDs and solar cells, defects also play a significant role in performance. In solar cells, defects such as cracks and lattice imperfections can lead to deteriorated current–voltage (*I*–*V*) characteristics, reducing energy conversion efficiency. These defects hinder the effective movement of electrons, increase non-radiative recombination, and decrease electrical power output [7, 8]. Similar defects can cause reduced light output and efficiency in LEDs [9, 10]. Therefore, a deep understanding and control of these defects are crucial for enhancing the performance and reliability of semiconductor devices.

In this context, deep level transient spectroscopy (DLTS) was first introduced by D. V. Lang in 1974 and has evolved into a widely used, multifunctional technique for characterizing semiconductor materials and devices [11–13]. It is suitable for a broad range of semiconductor devices, including Schottky and PN junctions, as well as metal–oxide–semiconductor (MOS) and metal–insulator–semiconductor (MIS) structures. DLTS provides essential defect parameters, such as thermal activation energy ( $E_a$ ), electron and hole capture cross-sections ( $\sigma_{n,p}$ ), and defect concentration ( $N_T$ ). DLTS is one of the most sensitive electrical measurement techniques, capable of detecting electrically active impurity concentrations down to  $10^{-5}$  times the substrate doping concentration. For example, if the substrate is doped at a concentration of  $10^{15} \text{ cm}^{-3}$ —a value considered typical—the resulting sensitivity would be  $10^{10} \text{ cm}^{-3}$ .

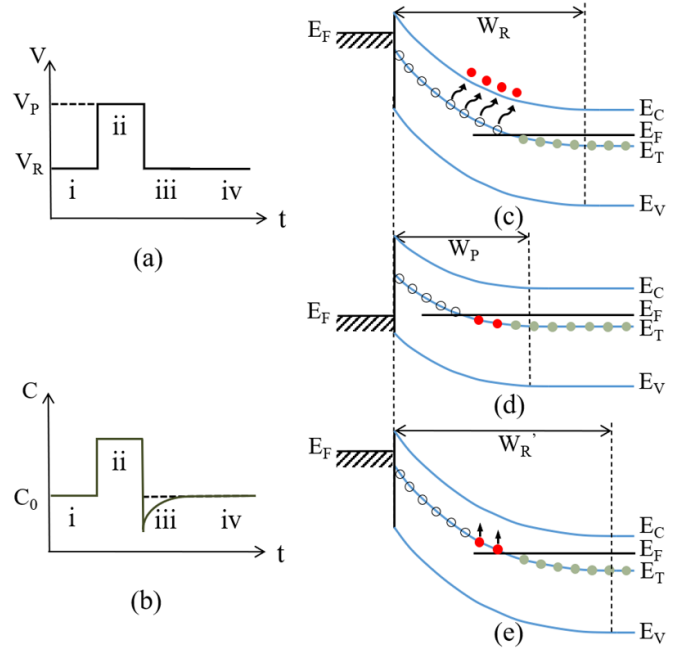


**Figure 1.** Energy band diagrams of an *n*-type Schottky contact under various bias voltages. (a) Represents the process of the applied pulse voltage over time, (b) shows the transient capacitance changes following the pulse voltage application, and (c)–(e) depict the physical processes before and after the application of the pulse voltage.

The theoretical foundation of DLTS is based on deep-level transient emission. To illustrate, consider *n*-type semiconductors and donor defect levels as an example, as depicted in figure 1. The figure illustrates the physical processes in an *n*-type semiconductor material forming a Schottky contact with metal, going through a reverse bias voltage (c), zero voltage pulse (d), and the state after the pulse is removed (e).

The Schottky contact is subjected to a reverse bias for a sufficient duration to establish thermal equilibrium, as illustrated in figure 1(c). At this steady state, the depletion width is increased to  $W_R$  and the mobile charges are swept out of the space charge region that all of the traps inside the depletion width tend to emit the occupied electrons and become empty. The depletion width can be calculated using the formula  $W = (2\epsilon (V_{bi} - V)/qN_d)^{1/2}$ , In this equation,  $\epsilon = \epsilon_s \epsilon_0$ , where  $\epsilon_s$  is the permittivity of the semiconductor and  $\epsilon_0$  is the permittivity in vacuum. Here,  $V_{bi}$  is the built-in potential,  $V$  is the applied bias, and  $q$  is the charge of an electron.  $N_d$  is the doping concentration, can be derived from the capacitance–voltage (*CV*) characteristics using the equation  $N_d = -2/qA^2 \epsilon (d(I/C^2)/dV)$ , where  $A$  is the contact area.

When the applied voltage switches from reverse bias to zero bias, as illustrated in figure 1(d). The depletion width of the semiconductor will decrease to  $W_p$  and electrons are recaptured by the deep levels in the band gap. This process is called the filling-up period of defect levels. As the pulse is turned off and the voltage transitions back from zero bias to reverse bias, the depletion width widens to  $W_R$  again, as

shown in figure 1(e). Within the depletion zone, conducting electrons are expelled, and the electrons captured by the traps will be gradually emitted back to the conduction band with an emission rate depending on the temperature. The thermal emission process is intricately linked to the physical characteristics of defects, leading to inevitable variations in the device's capacitance.

The dynamic processes of electron capture and emission in deep-level traps can be characterized by the capture cross-section  $\sigma_n$  and the emission rate  $e_n$ . According to the principle of detailed balance, the following relationship can be established [11]:

$$e_n = (\sigma_n \nu_{th} N_c / g_1) \exp\left(\frac{E_C - E_T}{kT}\right). \quad (1)$$

Here,  $\nu_{th}$  the average electron velocity,  $N_c$  is the effective state density in the conduction band,  $g_1$  is the degeneracy of the defect level, and the difference  $E_C - E_T$  specifies the relative position of the energy level in the bandgap with respect to the conduction band edge, essentially representing the activation energy. Analogous expressions can also be extrapolated for the capture and emission processes involving holes. The reciprocal of the emission rate is termed the emission time constant ( $\tau_e$ ) of the capacitance transient, typically following the relation:

$$C(t) = C_0 \left[ 1 - \frac{N_T}{2N_d} \exp\left(-\frac{t}{\tau_e}\right) \right]. \quad (2)$$

Here,  $C_0$  is the steady-state capacitance at the reverse bias  $V_R$ . For a sufficiently prolonged filling pulse duration, it describes the trap concentration  $N_T$ , nearly equal to  $2|\Delta C_0|N_d/C_0$ . Equation (2) illustrates the transient capacitance value in the space charge region after the bound electrons in the traps are emitted, corresponding to section 3 in figure 1(b). If the trap concentration is much lower than the total ionized doping concentration, i.e.  $N_T \ll N_d$ , this formula holds true [14].

While DLTS is a powerful tool for analyzing the capture and emission dynamics of deep-level traps, it also has some limitations.

Firstly, conventional DLTS methods are unable to precisely investigate the concentration-depth distribution of deep-level defects. This method is suitable for studying samples with uniformly distributed defect levels, providing an average defect concentration. However, in practical applications, the concentration-depth distribution of deep-level defects is often non-uniform. Typical examples include the end of range damage following ion implantation into silicon [15] or carbon contamination in epitaxial growth of GaN [16]. As device structures become increasingly complex, conducting a more detailed study of the concentration-depth distribution of deep-level defects becomes particularly important. Modern device structures involve intricate material layering and fabrication processes, where deep-level defects may exhibit a non-uniform distribution across different layers and interfaces.

Therefore, gaining accurate insights into the location and concentration distribution of these defects is crucial for optimizing device performance and enhancing reliability.

Secondly, conventional DLTS often overlooks the dependency of carrier emission rates on the electric field. Emission rates are influenced by the applied electric field through mechanisms such as the Poole–Frenkel effect, phonon-assisted tunneling, and direct tunneling. These three mechanisms are also associated with charge properties. Conventional DLTS assumes that field-enhanced emission of carriers indicates defects ionizing after emission, with the charge state of the defect opposite in sign to the charge state of the emitted carrier. This conventional criterion may lead to misleading conclusions. Further clarification of the charge state of defects is necessary to accurately assess the emission process of defects.

Lastly, conventional DLTS is unable to accurately identify defect structures. Defects in semiconductors mainly include point defects, extended defects, and surface states, among others. In the spectra of conventional DLTS, signals from these different types of defects may simultaneously appear, making it challenging to effectively identify defect structures. For example, in materials such as III–V arsenides, many types of defects have a high density. Extended defects trap free carriers, hindering their radiative recombination and consequently compromising the electrical and optical performance of devices. Therefore, the structural identification of these defects is crucial for further research. In modern semiconductor materials, the presence of complex defect structures and interface states underscores the growing urgency for advanced techniques capable of identifying defect structures.

In summary, as semiconductor materials and devices continue to advance, there is a growing demand for exploring deeper levels of defect information. Conventional DLTS methods have become inadequate in meeting these demands. Additionally, to achieve more accurate DLTS measurements, it is essential to minimize issues such as series resistance [17] and leakage current [18] during the sample preparation process. Consequently, this article aims to review and summarize the application of conventional DLTS techniques, particularly those that address the limitations of conventional methods. These techniques involve analyzing the concentration-depth distribution of deep defects, investigating the emission mechanisms of deep-level defects, and identifying defect microstructures. By providing comprehensive explanations of the principles, application domains, and advantages of these techniques, our objective is to offer a thorough understanding of deep-level defect analysis methods, with a specific emphasis on their applications in enhancing semiconductor device performance and reliability.

## 2. Defect spatial distribution

To measure the spatial distribution of defects, Lefevre and Schultz [19, 20] further advanced DLTS technology to develop double correlation DLTS (DDLTS). By recording DLTS signals generated by a series of different filling pulses and

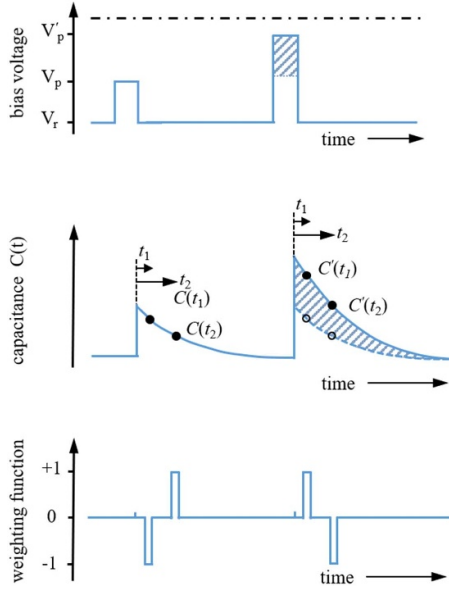


**Figure 2.** Schematic diagrams of the pulse shapes, capacitance signals, and corresponding weighting functions used in DDLTS. Reproduced from [19], with permission from Springer nature.

analyzing the differences between transient signals, it can be used to determine the spatial distribution of defects.

In the following, we will use two filling pulses ( $V_p$  and  $V'_p$ ) as examples to illustrate the derivation of the formula, as shown in figure 2. In the data processing of conventional DLTS, the DLTS signal is analyzed by sampling the capacitance difference at two time instants,  $t_1$  and  $t_2$ , during temperature scanning, i.e.  $\Delta C = C(t_1) - C(t_2)$ . However, during DDLTS measurement, the transient capacitance after two pulses is correlated by applying the same  $t_1$  and  $t_2$ , resulting in the respective differences  $\Delta C(t_1)$  and  $\Delta C(t_2)$  with a corresponding delay time [19, 20]. The correlated signal  $\Delta^2 C$  is obtained through a weighting function,

$$\Delta^2 C = \Delta C(t_1) - \Delta C(t_2) = (C'(t_1) - C(t_1)) \times -(C'(t_2) - C(t_2)) \quad (3)$$

In the correlation process mentioned above, an observation window  $x'_{fp} - x_{fp}$  is established within the space-charge region.  $x_{fp}$  (or  $x'_{fp}$ ) is the position where the trap level crosses the Fermi level at the end of the pulse  $V_p$  (or  $V'_p$ ), at this point, the width of the depletion region corresponds to  $x_p$  (or  $x'_p$ ). The positions  $x_{fp}$  and  $x'_{fp}$  are defined as  $x_{fp} = x_p - \lambda$  and  $x'_{fp} = x'_p - \lambda$ , respectively, where  $x_p = \varepsilon A / C$  and  $C$  measured at the pulse  $V_p$ ;  $\lambda$  is the distance from the edge of the depletion region to the point where the Fermi energy level intersects with the trap energy level [21],

$$\lambda = \left[ \frac{2\varepsilon (E_F - E_T)}{q^2 N_d} \right]^{1/2} \quad (4)$$

By forming the difference  $\Delta C(t)$  of the capacitance transient after the pulses, only the charge recovery process of the traps within the observation window is detected. The profile

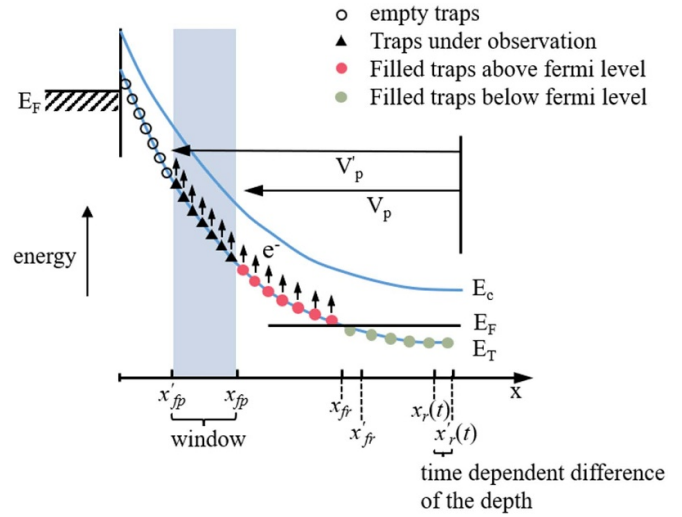


**Figure 3.** The schematic diagram of energy band bending at Schottky contacts, used to define the Fermi level crossing point and the observation window. Reproduced from [19], with permission from Springer nature.

analysis is conducted by adjusting the position of the observation window, which is accomplished through a series of incremental filling pulses while maintaining all other parameters constant, as illustrated in figure 3. The configuration of this observation window demonstrates significant advantages [19].

Initially, it is essential to note that all traps within the designated observation window are situated significantly above the Fermi level of the majority carriers. The transient characteristics observed are primarily governed by the thermal emission rate. Concurrently, the observation window is strategically positioned to avoid proximity to the Debye tail—a region characterized by the bending of electron or hole levels due to surface or interface electric fields. This bending has the potential to alter the occupancy state and energy level distribution of the traps. Occasionally, this phenomenon is referred to as ‘incomplete trap filling’. Neglecting this aspect could lead to significant errors [22].

Secondly, this setup ensures that the changes in the electric field across all observation windows are small, thereby effectively enhancing the reliability and accuracy of the measurement results. This is particularly crucial in scenarios where carrier emission is notably intensified by electric fields. Consequently, this methodology not only markedly improves the precision and reliability of the measurements but also underscores the unique advantages of DLTS in accurately characterizing deep-level defect concentration distributions.

The concentration distribution data in DDLTS is obtained by conducting measurements at the temperatures corresponding to the peak values observed in the DLTS spectrum. This process involves progressively increasing the filling pulse, followed by measuring the transients under a fixed reverse bias. The analysis involves examining the differences in transient amplitudes at each incremental step of the filling pulse voltage. From this analysis, profiles of the deep-level distribution can be determined. Lefevre proposed a relevant mathematical



model to represent this process [19], which can be expressed as:

$$n_T(x_{fp}) = 2 \exp(t_1/\tau) (\varepsilon A)^2 (n_0(x_r)) \frac{\Delta C(t_1)}{C_r^3(t_1)} \frac{1}{x_{fp}^2 - x_{fr}^2}, \quad (5)$$

where  $\tau$  is the time constant, equal to  $1/e_n$ , which can be derived from the Arrhenius plot.  $C_r$  is the space charge capacitance,  $n_0(x_r)$  is the shallow doping concentration at  $x_r$ , determined by standard differential CV-analysis,

$$n_0(x_r) = \frac{C_r^3}{q \varepsilon A^2} \frac{dV_r}{dC_r}, \quad (6)$$

where  $x_r$  is the boundary of the space charge region at the reverse voltage  $V_r$ , with  $x_r = \varepsilon A/C$  and  $C$  measured at the reverse voltage  $V_r$ .  $x'_r = x_r - (x_r^2/\Delta x)$ ;  $\Delta x = (\varepsilon A/\Delta C)$ .  $x_{fr}$  is the point where the trap level crosses the Fermi level under the reverse bias  $V_r$ . The condition  $x_{fr} = x_r - \lambda$  is satisfied. Similarly, it follows that  $x'_{fr} = x'_r - \lambda$ . It is worth noting that  $\lambda$  is independent of the applied voltage.

S. Loualiche has noted that the formula provided by Lefevre is based on the study of donor-like traps. When dealing with acceptor-like deep traps, it is necessary to modify Lefevre's expression to ensure its applicability [23].

$$n_T(x_{fp}) = e^{t/\tau} n_a(x_r) \times \frac{(x_r'^2 - x_r^2)}{\left( x_{fp}^2 - x_{fp}'^2 \right) + \frac{N_T}{n_T(x_{fp})} (x_{fr}'^2 - x_{fr}^2)}. \quad (7)$$

Hu *et al* [24] employed the DDLTS technique to investigate deep-level defects in nitrogen-doped *p*-type ZnSe epitaxial layers. This technique enables the selective measurement of signals originating solely from a very narrow and well-defined region of the depletion layer. By adjusting the pulse voltage  $V_p$ , while maintaining a constant reverse bias of  $V_r = -11$  V and a steady pulse-to-pulse increment  $\Delta V_p = 1.0$  V, the authors were able to vary the position and width of the measurement region.

The spatial distribution of trap concentrations obtained from these measurements is depicted in figure 4. It can be observed from the figure that the distribution patterns of traps  $HN_2$  and  $HN_3$  are quite similar. They increase gradually in the direction towards the substrate and then decrease sharply at approximately  $d = 0.45 \mu\text{m}$ . The researchers speculate that this phenomenon may be caused by weak emissions near the edge of the depletion layer, known as the 'edge region', which is defined by the intersection points of the trap and Fermi levels. Furthermore, they propose a hypothesis that both types of traps are related to nitrogen impurities. Unlike  $HN_2$  and  $HN_3$ , the concentration of the  $HN_1$  trap seems to increase near the surface of the sample. The authors believe that this is consistent with the hypothesis that  $HN_1$  may be related to selenium vacancies ( $V_{se}$ ), and it aligns with the notion that nitrogen impurities tend to diffuse out of the sample.

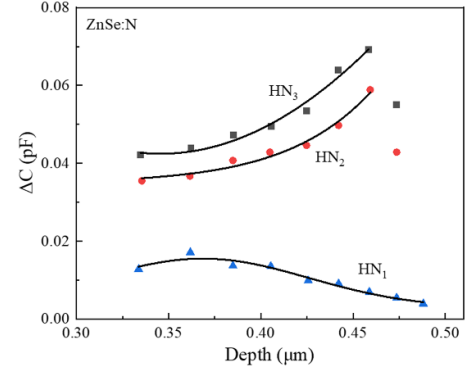


**Figure 4.** The concentration distributions of traps  $HN_1$ ,  $HN_2$ , and  $HN_3$  as measured by DDLTS. Reprinted from [24], with the permission of AIP Publishing.

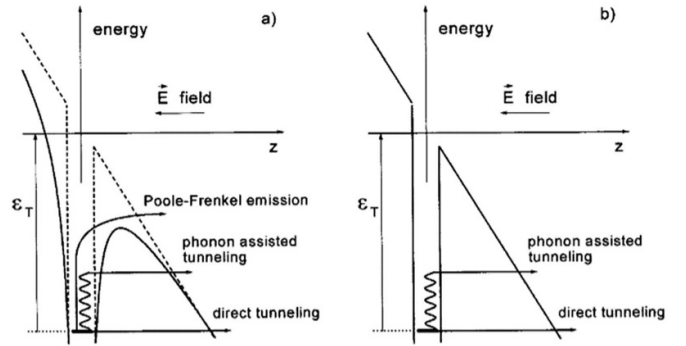


**Figure 5.** Schematic diagram of the electron emission barrier for deep-level defects in an external electric field: (a) for charged and (b) for neutral impurities. Reprinted with permission from [33]. Copyright (2000) American Chemical Society.

### 3. Emission mechanism

The assessment of defect emission mechanisms helps in gaining a deeper understanding of how defects influence carriers. It is commonly observed that the emission rate increases with the electric field, typically indicating charged defects. However, the underlying physics involves multiple mechanisms that warrant further discussion. The most prevalent emission mechanisms can be broadly classified into two types: the Poole–Frenkel effect [25–28] and phonon-assisted tunneling [29–32]. The Poole–Frenkel effect occurs exclusively in charged impurities. It involves the reduction of the Coulomb barrier under the influence of an external electric field, thereby facilitating the thermal emission of carriers from traps and leading to an increased emission rate. In contrast, phonon-assisted tunneling, which is applicable to both charged and neutral impurities, dominates under high electric fields. In this mechanism, phonon excitation assists carriers in overcoming barriers, thereby enhancing the emission rate [33], as illustrated in figure 5.

Another method in DDLTS is required for this study, which involves maintaining the height of the filling pulse constant while gradually adjusting the magnitude of the reverse bias, as illustrated in figure 6. As the reverse voltage increases, the

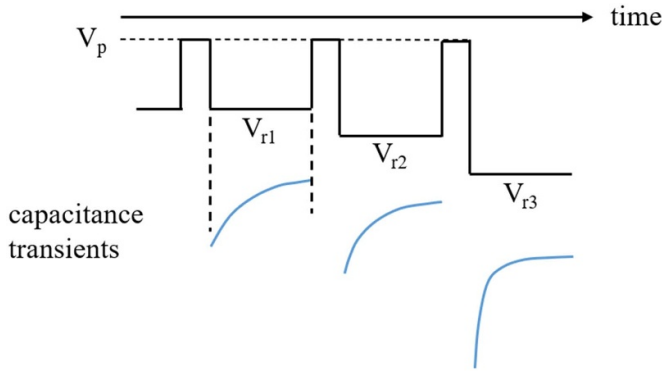


**Figure 6.** The impact of reverse bias variation on the DLTS signal.

electric field experienced by the traps also increases, resulting in an enhanced emission rate. Further analysis of this change in the emission rate is then conducted.

These two mechanisms can be differentiated using a simple criterion. In the Poole–Frenkel effect, the logarithm of the emission rate is directly proportional to the square root of the electric field [25, 33, 34], which can be expressed as:

$$e(E)/e(0) \propto \exp(\varepsilon_{PF}/k_B T), \quad (8)$$

where  $e(E)$  is the emission rate as a function of the electric-field strength  $E$  and the lowering of the barrier  $\varepsilon_{PF}$  is given by

$$\varepsilon_{PF} = 2\sqrt{\frac{Zq^3 E}{\chi}}. \quad (9)$$

Here,  $Z$  is the charge of the center,  $q$  is the electron charge,  $E$  is the electric-field strength, and  $\chi$  is the dielectric constant. Conversely, in the phonon-assisted tunneling mechanism, the logarithm of the emission rate is directly proportional to the square of the electric field [33], which can be represented as:

$$e(E)/e(0) = \exp\left(\frac{E^2}{E_{cf}^2}\right), \quad (10)$$

where  $E_{cf}$  is the characteristic field strength, which is given by the following equation:

$$E_{cf} = \sqrt{\frac{3m^* \hbar}{q^2 \tau_2^3}}, \quad (11)$$

where  $m^*$  is the effective mass of charge carriers, and  $\tau_2$  is the tunneling time, given by ([35]).

When analyzing the charge states of defects, we can observe the dependency of carrier emission rates on the applied electric field strength. If the observed phenomena align with the Poole–Frenkel effect, this typically indicates the presence of charged impurities. If the phenomena correspond to phonon-assisted tunneling mechanisms, it suggests that the carriers may originate from either neutral or charged impurities. However, accurately assigning the charge state of defects still requires additional experimental data.

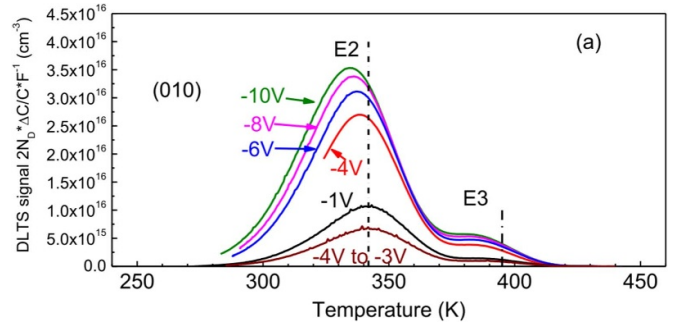


**Figure 7.** The DLTS spectra of Sn-doped  $\beta$ -Ga<sub>2</sub>O<sub>3</sub> crystal samples under different reverse biases. Reproduced from [36]. © IOP Publishing Ltd. All rights reserved.

A.Y. Polyakov and others [36] conducted research using DLTS spectroscopy on Sn-doped  $\beta$ -Ga<sub>2</sub>O<sub>3</sub> crystal samples. The samples underwent reverse bias ranging from  $-1$  V to  $-10$  V, while the forward bias pulse was set at  $0$  V. As shown in figure 7, the y-axis of the figures is  $2N_D (\Delta C/C) F^{-1}$ , where  $\Delta C$  is the difference of the capacitance decay curves at time windows  $t_1$  and  $t_2$ ,  $C$  is the steady capacitance, and  $F^{-1}$  is the spectrometer function converting  $\Delta C$  values into the complete capacitance relaxation values. The authors observed two main electron trap peaks, named E2(in Ga<sub>2</sub>O<sub>3</sub>) and E3(in Ga<sub>2</sub>O<sub>3</sub>). With the increase in reverse bias, the peak values of these traps shifted towards lower temperatures. This trend is induced by the change in the electric field strength within the semiconductor.

Based on equations (8) and (10), the researchers plotted the logarithm of the normalized emission rate against the electric field, as illustrated in figure 8. For the E2(in Ga<sub>2</sub>O<sub>3</sub>) trap, a linear relationship between its emission rate and the square of the electric field strength was observed at high electric fields, suggesting that phonon-assisted tunneling is the primary emission mechanism. For the E3(in Ga<sub>2</sub>O<sub>3</sub>) trap, the emission rate exhibited a linear relationship with the square root of the electric field strength, indicating that it is primarily influenced by the Poole–Frenkel effect. Through analysis, the authors conclude that the E2(in Ga<sub>2</sub>O<sub>3</sub>) trap exhibits characteristics consistent with the known acceptor traits corresponding to the Fe<sup>3+</sup>/Fe<sup>2+</sup> charge transition acceptor level, while the emission behavior of the E3(in Ga<sub>2</sub>O<sub>3</sub>) trap aligns with the Poole–Frenkel effect, indicating it is a deep-level donor defect.

#### 4. Defect structure identification

Understanding the structure of defects is crucial for devising methods to control them. To effectively identify defect structures, two main methods are employed. First, by keeping the filling pulse constant while simultaneously increasing the reverse voltage [37, 38], this method can effectively differentiate between interface state defects and bulk defects. Second, the utilization of variable pulse width DLTS enables a more precise differentiation between point defects and extended defects within bulk defects by adjusting the pulse width

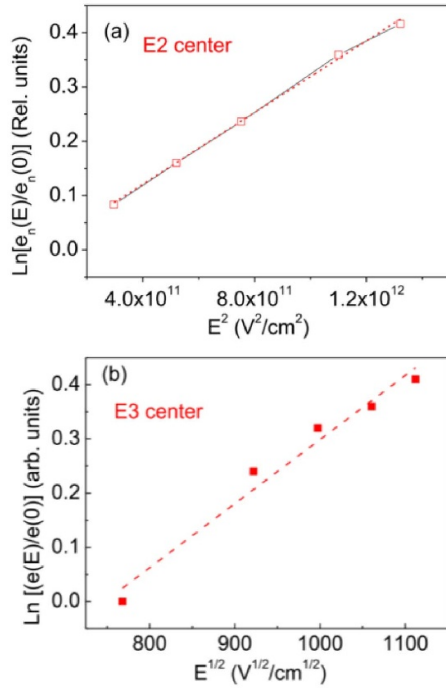


**Figure 8.** The logarithm of the normalized emission rate and its linear fit with (a)  $E^2$ , (b)  $E^{1/2}$ . Reproduced from [36]. © IOP Publishing Ltd. All rights reserved.

[39–42]. These two methods play a key role in identifying defect structures.

#### 4.1. Interface states and bulk defects

In the previous discussions, modifying the reverse bias was demonstrated as a method to distinguish the defect emission mechanisms. This approach is equally crucial in distinguishing between bulk defects and interface states [37, 38]. Typically, there are two methods used to distinguish these types of defects. The first method involves measuring the DLTS spectra of MIS structures that include interface states, followed by removing the metal and insulator layers to deposit Schottky contacts. This process allows obtaining DLTS spectra that only contain bulk defects. However, this method is destructive. The second method examines whether the DLTS signal peak shape and peak values change with the filling pulse voltage. It is generally believed that the peak shape and values associated with bulk defects remain constant, whereas those related to interface states change. This is based on the assumption that defects do not have a strong dependency on the electric field, which may not apply to all defects [43, 44]. Coelho *et al* [38] observed distinct characteristics between bulk defects and interface states, which can be utilized to determine the type of defect.

Initially, the authors validated the second approach, which involved altering the filling pulse voltage while keeping the reverse voltage constant to measure the DLTS spectra. This method proved to be inapplicable for bulk traps with a strong

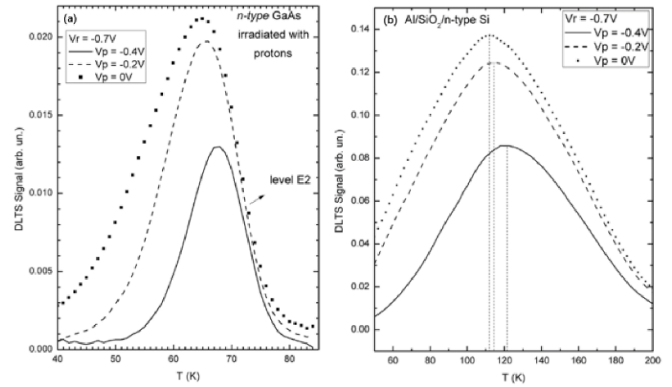


**Figure 9.** The DLTS spectra for (a) bulk traps in  $n$ -type GaAs and (b) interface states in Al/SiO<sub>2</sub>/Si MIS capacitors under different  $V_p$ . Reproduced from [38]. © IOP Publishing Ltd. All rights reserved.

dependency on the electric field, such as the E2(in GaAs) trap [45]. As illustrated in figure 9, the authors observed consistent behavior where the peak shape changed, and the maximum value shifted towards lower temperatures. This observation indicates that the previously described method is not effective in distinguishing between interface state peaks and bulk defect peaks that are highly dependent on the electric field.

Subsequently, the authors introduce a new method in the article, which involves keeping the filling pulse constant while increasing the reverse bias. This approach more accurately distinguishes between bulk defects and interface state traps without damaging the sample. Firstly, considering the case of bulk defects: the method involves keeping  $V_p$  constant while gradually increasing the reverse bias from  $V_r$  to  $V_r'$ . At this point, the depletion depth under the reverse bias changes from  $x_1$  to  $x_1'$ , while  $x_2$  remains constant. Considering a sufficiently long filling pulse, it can be demonstrated that deep-level related traps in the depth region between  $x_1 - \lambda$  and  $x_2 - \lambda$  will be filled during the pulse and will emit the trapped carriers after it [46], as shown in figure 10. This results in an enhanced electric field within the  $V_r/V_p/V_r$  region of active traps and introduces a new region of active traps near the depletion depth  $x_1'$ , as shown in figures 10(a) and (b). Due to the field dependence of the emission rate of E<sub>2</sub>(in GaAs) defects, the spectral graph shows a shift of the peak towards the lower temperature region, as illustrated in figure 10(c).

In the case of interface states, when the reverse voltage increases from  $V_r$  to  $V_r'$ , deeper states are activated, as depicted in figures 11(a) and (b). Without considering the variation in capture cross-section, these states emit more slowly, causing the peak in the spectral graph to shift towards higher temperature regions, as shown in figure 11(c).

Consequently, the authors emphasize the key characteristic of this method: for bulk defects, the peak's maximum value shifts towards lower temperatures; whereas for interface states, the peak's maximum value moves towards higher temperatures. This distinction mechanism offers a more precise and non-destructive method for identifying defect structures.

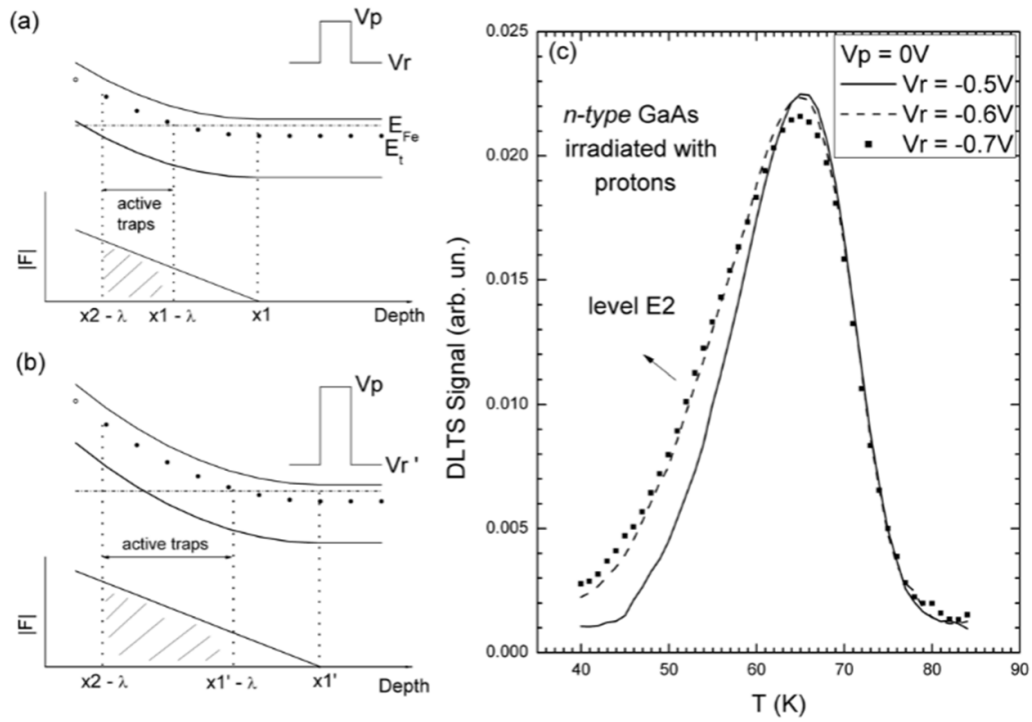


**Figure 10.** (a) Active traps and the corresponding electric field regions at  $V_r$ , (b) at  $V_r'$ , and (c) the measured spectra of the E2 (in GaAs) energy level under different reverse bias voltages. Reproduced from [38]. © IOP Publishing Ltd. All rights reserved.

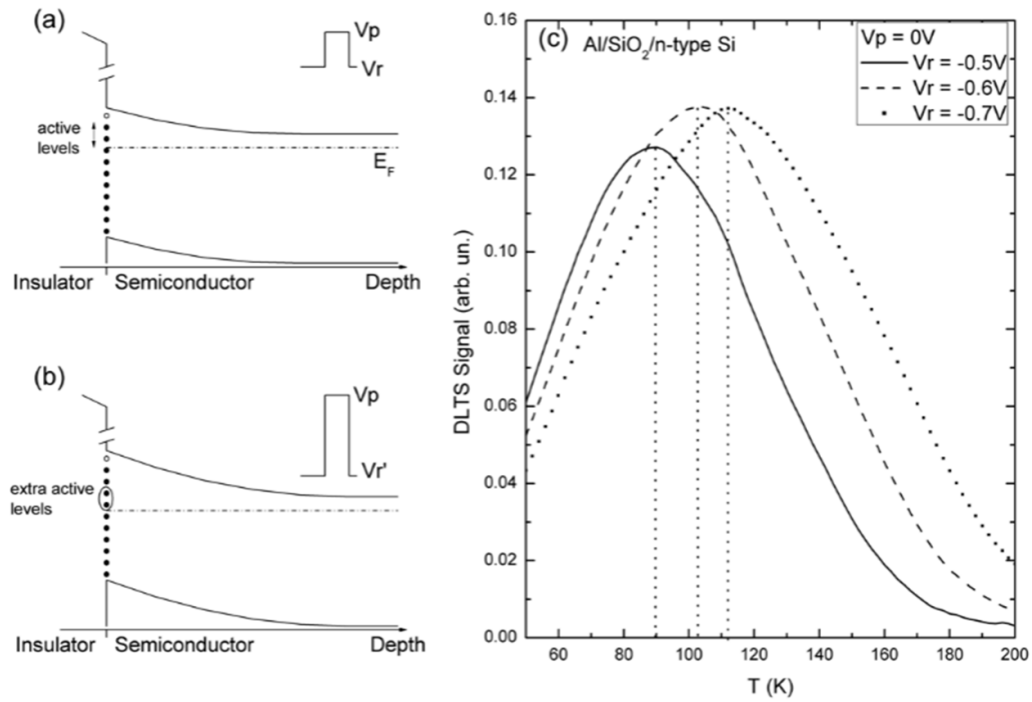


**Figure 11.** (a) Active traps at  $V_r$ , (b) active traps at  $V_r'$ , and (c) the measured spectra of MOS capacitors under different reverse bias voltages. Reproduced from [38]. © IOP Publishing Ltd All rights reserved.



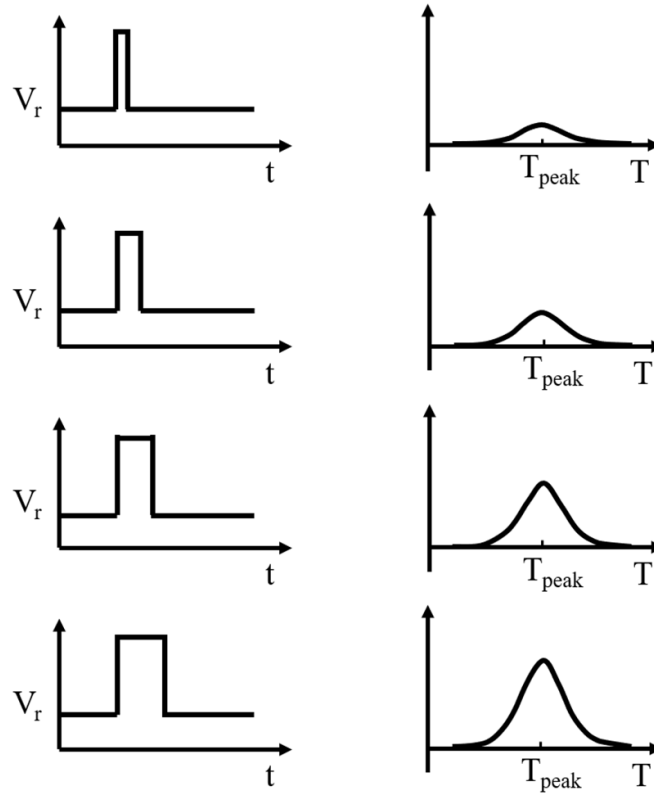


**Figure 12.** The impact of pulse width variation on the DLTS signal.

In the conclusion of the paper, the authors mention that this new method may encounter challenges when dealing with non-uniform distributions of bulk traps or interface states that have significant changes in their electron (or hole in *p*-type semiconductors) capture cross-sections. To mitigate the impacts of these issues, the authors suggest adopting more refined strategies for adjusting pulses and reverse biases. Additionally, the authors note that the study did not consider interface states with strong electric field dependencies. If such dependencies exist, the emission rates of these interface states would increase with the increase of  $|V_r|$ . In such cases, if the electric field dependency is strong enough, the maximum value of the DLTS peak might shift towards lower temperatures. Therefore, using this method alone may not be sufficient to differentiate interface states from bulk traps. The authors emphasize that further research and exploration are required for more accurate identification of these structures.

#### 4.2. Point defects and extended defects

The Pulse Width Dependent DLTS technique has garnered significant attention for its ability to differentiate between point defects and extended defects. By employing various filling pulse widths under constant temperature conditions, this method generates a series of DLTS spectra. This approach highlights the crucial role of filling pulse width in

experimental design and further elucidates the intricate interactions between carriers and defect levels.

Longer filling pulse widths enable carriers to interact with multiple defect levels for an extended duration, leading to a robust signal response. In contrast, shorter filling pulse widths limit the interaction of carriers with specific defect levels to a shorter duration, thus producing a weaker signal [11, 47, 48], as illustrated in figure 12. By analyzing experimental data obtained under different filling pulse widths, the pulse width dependent DLTS technique can provide in-depth insights into the characteristics of defect levels, thereby effectively distinguishing between point defects and extended defects.

For point defects, according to the equation below, it can be observed that the capture cross-section shows a linear dependence on the logarithm of the capacitance term, which functions as a pulse width parameter [49–51]:

$$\ln \left( \frac{\Delta C_\infty - \Delta C_t}{\Delta C_\infty} \right) = -\sigma_n \cdot v_{th} \cdot n \cdot t_p, \quad (12)$$

where  $\Delta C_\infty$  is the variation in the capacitance after a filling pulse long enough to fill all the traps, and  $\Delta C_t$  is the variation in the capacitance after a filling pulse of duration  $t_p$ ,  $\sigma_n$  is the trap capture cross-section,  $n$  is the carrier concentration,  $t_p$  is the filling pulse width,  $v_{th}$  is the thermal velocity. Furthermore, many researchers conduct measurement studies of the direct capture cross-section based on this formula [52–54].

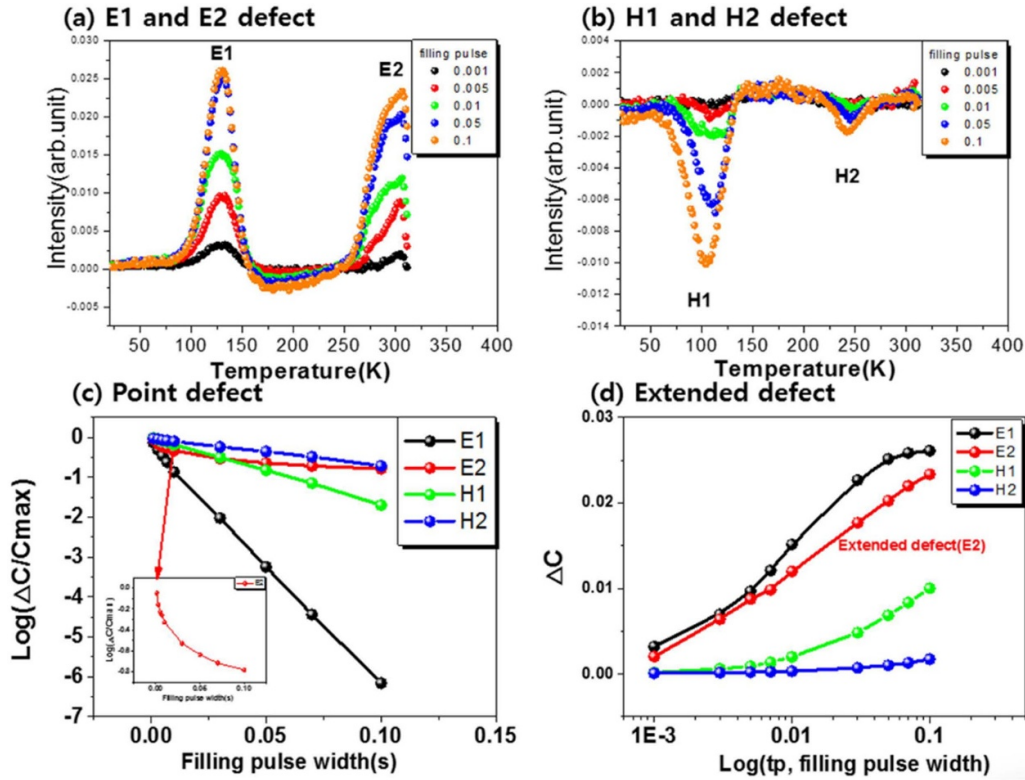


**Figure 13.** The behavior of the DLTS spectrum with changes in filling pulse width is as follows: (a) electron defects E1(in CIGSS) and E2(in CIGSS) in the forward region (from 0.2 V to 0.4 V), (b) hole defects H1 and H2 in the reverse region (from  $-0.6$  V to  $-0.4$  V), and (c) point defects and (d) extended defects for levels E1(in CIGSS), E2(in CIGSS), H1, and H2. Reproduced from [49]. CC BY 4.0.

When deviations from this relationship occur, it may indicate the presence of extended defects. For extended defects, the DLTS signal should exhibit a logarithmic dependence on the filling pulse duration [41, 50, 51, 55–57]:

$$\Delta C_m \propto \log(t_p), \quad (13)$$

where  $\Delta C_m$  is the amplitude of the DLTS signal.

Sung Heo and others [49] utilized DLTS technology to examine the types of defects in Cu(InGa)(SeS)<sub>2</sub>. Figures 13(a) and (b) illustrate the correlation of the DLTS spectra of electron defects E1(in CIGSS) and E2(in CIGSS) in the forward region, and hole defects H1 and H2 in the reverse region, with filling pulse width. Additionally, figures 13(c) and (d) also present the scenarios of point defects and extended defects for peaks E1(in CIGSS), E2(in CIGSS), H1, and H2. Notably, when analyzed using equation (12), the E1(in CIGSS), H1, and H2 defect peaks exhibit a significant linear relationship, as shown in figure 13(c). Based on this finding, E1(in CIGSS), H1, and H2 can be classified as point defects. On the other hand, the E2(in CIGSS) peak does not align well with equation (12) but exhibits a strong linear relationship in the analysis linked to equation (13). The researchers inferred

that the E2(in CIGSS) peak might represent an extended defect, such as a grain boundary-related defect, dislocation, or vacancy.

O S Elsherif and colleagues [50] conducted high-resolution DLTS experiments to meticulously explore the capture and filling behavior of deep-level defects in boron-doped diamond. This study achieved precise analysis of the dynamic characteristics of defects by varying the filling pulse width. Experimental parameters included exploring deep-level characteristics within a filling pulse width range of 0–40 ms under a reverse bias of  $-3$  V and a filling pulse of  $-0.5$  V, as illustrated in figure 14. Data for levels E1(in Diamond), E2(in Diamond), and E3(in Diamond) were recorded at 170 K, 360 K, and 250 K, respectively. When the E3(in Diamond) defect was analyzed using equation (12), it exhibited a significant linear relationship, indicating that these defects are isolated point defects, likely associated with specific defect centers in boron-doped diamond. For defects E1(in Diamond) and E2(in Diamond), their DLTS signals exhibited a linear relationship with the logarithm of the filling pulse width, which supports the hypothesis that they exist as extended defects. This behavior is distinctly different from that of point defects.

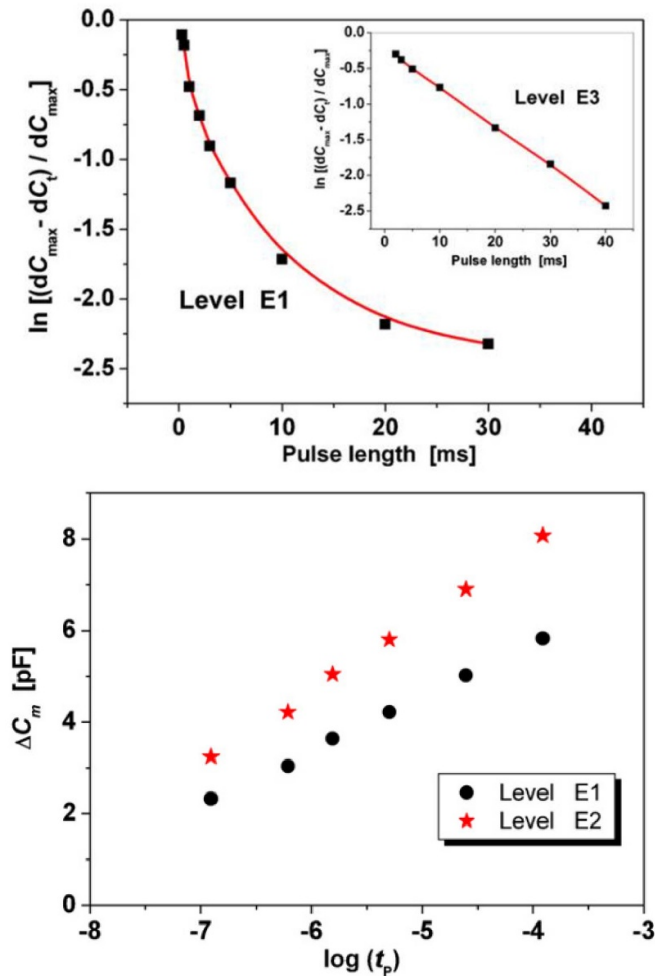


**Figure 14.** (a) the capacitance changes associated with defects at locations E1(in Diamond) and E3(in Diamond) are functionally related to the length of the filling pulse; (b) the DLTS signal serves as a function of the logarithm of the fill width for defects at locations E1(in Diamond) and E2(in Diamond) within the sample. Reproduced from [50]. © IOP Publishing Ltd. All rights reserved.

## 5. Conclusion

This review critically examines three principal limitations of conventional DLTS technology: its inability to reveal the concentration and depth distribution of deep-level defects, the failure to consider the dependence of carrier emission rates on the electric field; and thirdly and the lack of precision in identifying defect structures. To overcome these challenges, the article introduces three advanced functionalities of DLTS: variable filling pulse amplitude, variable reverse bias and pulse width dependent DLTS.

The variable filling pulse amplitude approach focuses on exploring the concentration and depth distribution of defects, aiming to reveal the spatial distribution of deep-level defects within materials. The variable reverse bias approach is employed to analyze traps whose carrier emission capture processes are highly dependent on the applied electric field. By plotting the logarithm of the emission rate against the square root and the square of the electric field strength, this method effectively distinguishes between the Poole–Frenkel effect and phonon-assisted tunneling mechanisms. Additionally, the varying reverse bias can distinguish between interface states

and bulk defects by analyzing the trend of peak shifts with temperature changes.

Variable pulse width DLTS, by adjusting the duration of the filling pulse and then observing the linear relationship between the DLTS signal and the pulse width, can effectively distinguish between point defects and extended defects. The combined application of these two methods offers a comprehensive perspective for an in-depth understanding of the nature and behavior of defects. This contributes to enhancing semiconductor device performance and reliability, bringing progress and innovation to the field of deep-level defect research.

## Data availability statement

All data that support the findings of this study are included within the article (and any supplementary files).

## Acknowledgment

All the authors gratefully acknowledge the National Natural Science Foundation of China (62004021, 62374023).

## ORCID iD

Zilan Wang  <https://orcid.org/0000-0002-2741-5746>

## References

- [1] Euvrard J, Yan Y and Mitzi D B 2021 *Nat. Rev. Mater.* **6** 531–49
- [2] Andriotis A N and Menon M 2015 *J. Appl. Phys.* **117** 125708
- [3] McCluskey M D and Janotti A 2020 *J. Appl. Phys.* **127** 190401
- [4] Bennett B R, Magno R, Boos J B, Kruppa W and Ancona M G 2005 *Solid-State Electron.* **49** 1875–95
- [5] Singh R, Lenka T R, Panda D K, Velpula R T, Jain B, Bui H Q T and Nguyen H P T 2020 *Mater. Sci. Semicond. Process.* **119** 105216
- [6] Zhao J, Chen Q, Chen C, Chen Z, Liu Z and Zhao G 2022 *Sci. Rep.* **12** 16922
- [7] Marques Lameirinhas R A, P. Correia V, Bernardo C, N. Torres J P, Veiga H I and Mendonça Dos Santos P 2023 *Sci. Rep.* **13** 12490
- [8] Paggi M, Berardone I, Infuso A and Corrado M 2014 *Sci. Rep.* **4** 4506
- [9] Booker E P *et al* 2017 *J. Am. Chem. Soc.* **139** 18632–9
- [10] Armstrong A, Henry T A, Koleske D D, Crawford M H, Westlake K R and Lee S R 2012 *Appl. Phys. Lett.* **101** 162102
- [11] Lang D V 1974 *J. Appl. Phys.* **45** 3023–32
- [12] Peaker A R, Markevich V P and Coutinho J 2018 *J. Appl. Phys.* **123** 161559
- [13] Simoen E, Lauwaert J and Vrielinck H 2015 *Semicond. Semimet.* **91** 205–50
- [14] Schroder D K 2015 *Semiconductor Material and Device Characterization* section 5.3.2. (Wiley)
- [15] Listebarger J K, Jones K S and Slinkman J A 1993 *J. Appl. Phys.* **73** 4815–9
- [16] Seager C H, Wright A F, Yu J and Götz W 2002 *J. Appl. Phys.* **92** 6553–60
- [17] Broniatowski A, Blossie A, Srivastava P C and Bourgoin J C 1983 *J. Appl. Phys.* **54** 2907–10
- [18] Wakimoto H, Matsumoto T, Yano K and Muranaka T 2020 *AIP Adv.* **10** 125301
- [19] Lefevre H and Schulz M 1977 *Appl. Phys.* **12** 45–53
- [20] Lefevre H and Schulz M 1977 *IEEE Trans. Electron Devices* **24** 973–8
- [21] Zohta Y and Watanabe M O 1982 *J. Appl. Phys.* **53** 1809–11
- [22] Rockett P I and Peaker A R 1982 *Appl. Phys. Lett.* **40** 957–9
- [23] Loualiche S, Nouailhat A and Guillot G 1982 *Solid State Commun.* **44** 41–45
- [24] Hu B, Karczewski G, Luo H, Samarth N and Furdyna J K 1993 *Appl. Phys. Lett.* **63** 358–60
- [25] Frenkel J 1938 *Phys. Rev.* **54** 647
- [26] Hartke J L 1968 *J. Appl. Phys.* **39** 4871–3
- [27] Simmons J G 1967 *Phys. Rev.* **155** 657
- [28] Yeargan J R and Taylor H L 1968 *J. Appl. Phys.* **39** 5600–4
- [29] Karpus V 1986 *Soviet J. Exp. Theor. Phys. Lett.* **44** 430–3
- [30] Chynoweth A G, Logan R A and Thomas D E 1962 *Phys. Rev.* **125** 877
- [31] Makram-Ebeid S and Lannoo M 1982 *Phys. Rev. B* **25** 6406
- [32] Martin P A, Streetman B G and Hess K 1981 *J. Appl. Phys.* **52** 7409–15
- [33] Ganichev S D, Ziemann E, Prettl W, Yassievich I N, Istratov A A and Weber E R 2000 *Phys. Rev. B* **61** 10361
- [34] Trushin M, Vyvenko O, Vdovin V and Kittler M 2011 *J. Phys.: Conf. Ser.* **281** 012009
- [35] Ganichev S D, Yassievich I N, Prettl W, Diener J, Meyer B K and Benz K W 1995 *Phys. Rev. Lett.* **75** 1590
- [36] Polyakov A Y, Lee I, Smirnov N B, Shchemerov I V, Vasilev A A, Chernykh A V and Pearton S J 2020 *J. Phys. D: Appl. Phys.* **53** 304001
- [37] Lechaux Y, Chen Y, Minj A, Sánchez F, Herranz G, Méchin L and Guillet B 2022 *Appl. Phys. Lett.* **121** 081904
- [38] Coelho A, Adam M C and Boudinov H 2011 *J. Phys. D: Appl. Phys.* **44** 305303
- [39] Fang Z, Look D C, Kim D H and Adesida I 2005 *Appl. Phys. Lett.* **87** 182115
- [40] Fang Z, Claflin B, Look D C, Green D S and Vetury R 2010 *J. Appl. Phys.* **108** 063706
- [41] Grillot P N, Ringel S A, Fitzgerald E A, Watson G P and Xie Y H 1995 *J. Appl. Phys.* **77** 3248–56
- [42] Evans-Freeman J H, Emiroglu D, Vernon-Parry K D, Murphy J D and Wilshaw P R 2005 *J. Phys.* **17** S2219
- [43] Schroder D K 2006 *Semiconductor Material and Device Characterization* (Wiley) p 101
- [44] Yamasaki K, Yoshida M and Sugano T 1979 *Jpn. J. Appl. Phys.* **18** 113
- [45] Coelho A and Boudinov H 2008 *Phys. Rev. B* **77** 235210
- [46] Blood P and Orton J W 1992 *Techniques of Physics* i–xxiii
- [47] Vuillaume D, Bourgoin J C and Lannoo M 1986 *Phys. Rev. B* **34** 1171
- [48] Wang C W, Wu C, Boone J L and Balestra C L 1993 *J. Electron. Mater.* **22** 165–70
- [49] Heo S *et al* 2016 *Sci. Rep.* **6** 30554
- [50] Elsherif O S, Vernon-Parry K D, Evans-Freeman J H and May P W 2012 *Semicond. Sci. Technol.* **27** 65019
- [51] Duc T T, Pozina G, Janzén E and Hemmingsson C 2013 *J. Appl. Phys.* **114** 153702
- [52] Ali A, Shafi M and Majid A 2006 *Phys. Scr.* **74** 450
- [53] Shafi M, Mari R H, Khatab A, Taylor D and Henini M 2010 *Nanoscale Res. Lett.* **5** 1948–51
- [54] Henry C H and Lang D V 1977 *Phys. Rev. B* **15** 989
- [55] Figielski T 1978 *Solid-State Electron.* **21** 1403–12
- [56] Wosiński T 1989 *J. Appl. Phys.* **65** 1566–70
- [57] Omiling P, Weber E R, Montelius L, Alexander H and Michel J 1985 *Phys. Rev. B* **32** 6571